

Article

The First Application of a $\text{Gd}_3\text{Al}_2\text{Ga}_3\text{O}_{12}:\text{Ce}$ Single-Crystal Scintillator to Neutron Radiography

Kazuhisa Isegawa ^{1,*}, Daigo Setoyama ², Hidehiko Kimura ² and Takenao Shinohara ¹¹ Japan Atomic Energy Agency, Tokai 319-1195, Japan; takenao.shinohara@j-parc.jp² Toyota Central R&D Laboratories, Nagakute 480-1192, Japan; daigo@mosk.tytlabs.co.jp (D.S.); hdkimura@mosk.tytlabs.co.jp (H.K.)

* Correspondence: kazuhisa.isegawa@j-parc.jp

Abstract: Neutron radiography is regarded as complementary to X-ray radiography in terms of transmittance through materials, but its spatial resolution is still insufficient. In order to achieve higher resolution in neutron imaging, several approaches have been adopted, such as optical magnification and event centroiding. In this paper, the authors focused on modification of the scintillator. A $\text{Gd}_3\text{Al}_2\text{Ga}_3\text{O}_{12}:\text{Ce}$ single-crystal scintillator was applied to neutron radiography for the first time and a spatial resolution of 10.5 μm was achieved. The results indicate that this material can be a powerful candidate for a new neutron scintillator providing a resolution in micrometer order by optimizing the optical system and increasing the scintillator luminosity.

Keywords: neutron radiography; neutron imaging; neutron scintillator; gadolinium aluminium gallium garnet



Citation: Isegawa, K.; Setoyama, D.; Kimura, H.; Shinohara, T. The First Application of a $\text{Gd}_3\text{Al}_2\text{Ga}_3\text{O}_{12}:\text{Ce}$ Single-Crystal Scintillator to Neutron Radiography. *J. Imaging* **2021**, *7*, 232. <https://doi.org/10.3390/jimaging7110232>

Academic Editors: Raimondo Schettini, Anton Tremsin and Anders Kaestner

Received: 21 September 2021
Accepted: 1 November 2021
Published: 2 November 2021

Publisher's Note: MDPI stays neutral with regard to jurisdictional claims in published maps and institutional affiliations.



Copyright: © 2021 by the authors. Licensee MDPI, Basel, Switzerland. This article is an open access article distributed under the terms and conditions of the Creative Commons Attribution (CC BY) license (<https://creativecommons.org/licenses/by/4.0/>).

1. Introduction

Neutron radiography is a nondestructive method to observe the inside of samples. X-ray radiography is a similar and better-known technique but complementary in principle to neutron radiography. The X-ray cross section of each element is almost proportional to the squared atomic number, whereas for neutrons, it shows complex relationships. For example, neutrons penetrate metal structures but not hydrogen and lithium, so neutron radiography is suitable for the observation of fuel cells and Li-ion batteries [1,2]. However, the spatial resolution of neutron radiography is several orders of magnitude lower than that of X-ray radiography in terms of the maximum achievable value. Realization of both high resolution and high brightness expands the application range of neutron radiography. For example, the elemental distribution and behavior inside a multi-material sample composed of resins and metals can be observed at the same micrometer order.

Many demands exist for high-spatial-resolution neutron radiography of less than 10 μm , and various approaches are being developed to improve the resolution of neutron radiography: optical magnification [3–5], event centroiding [6–8], track recording [9,10], and neutron focusing techniques [11]. Optical magnification systems have been recently developed by the Paul Scherrer Institut (PSI) group, achieving resolutions of 10 μm by a fiber optics taper [3] and 5 μm by a neutron microscope [4,5]. The event centroiding process has been conducted at ISIS, LANSCE, and NIST [6–8]. As a result, a very high resolution of 2 μm has been achieved at NIST [8].

On the other hand, exploration of high-performance scintillators can also be an approach to achieve higher resolution imaging. The optical characteristics of scintillators also greatly affect the quality of obtained images because, in many cases, the spread of the bright points in the scintillator initially defines the resolution. Several types of powder scintillators, for example, $^6\text{LiF}/\text{ZnS}$ and gadolinium oxysulfide, $\text{Gd}_2\text{O}_2\text{S}:\text{Tb}$, named P43 or Gadox, have been mostly used for neutron radiography. The resolution and luminosity of the powder scintillators are in a trade-off relationship, that is, a thicker scintillator plate

brings about a higher luminosity, whereas the resolution becomes lower due to photon scattering inside the scintillator [12]. Consequently, most high-resolution imaging employs a Gadox scintillator enriched with the ^{157}Gd isotope because it exhibits the largest absorption cross section for low-energy neutrons and, hence, it is possible to make a very thin scintillator [3–5,13]. We have been interested in another promising candidate, a transparent single-crystal scintillator composed of elements with large neutron absorption cross sections, which is expected to provide both high resolution and high luminosity due to smaller photon scattering and attenuation inside than those for powder scintillator materials, irrespective of its thickness [12].

Previously, the Helmholtz-Zentrum Berlin group tested a transparent $\text{Gd}_3\text{Ga}_5\text{O}_{12}:\text{Eu}$ (GGG) single-crystal scintillator [14], but no subsequent studies have been reported after that. Recently, a single-crystal scintillator, $\text{Gd}_3\text{Al}_2\text{Ga}_3\text{O}_{12}:\text{Ce}$ (GAGG), has been developed by Yoshikawa and coworkers [15,16], and it is widely utilized for X-ray radiography because of its high luminosity and fast decay time for X-rays [17]. Because GAGG contains a high amount of Gd atoms like GGG and shows good optical transparency for the emitted light with a wavelength of 520 nm, it is expected to be utilized for high-resolution neutron-imaging applications. The decay time of GAGG is 0.2 μs [17], while that of GGG is 800 μs [18]. The short decay time of GAGG is very suitable for the energy-resolved neutron imaging using the pulsed neutron beam, in which the neutron energy is deduced by the time-of-flight method and a fine temporal resolution is required. However, the application of a GAGG single crystal to neutron detection is very limited [19], and, to our knowledge, no previous neutron-imaging study using it exists.

In this study, we applied a transparent single-crystal scintillator GAGG to neutron imaging for the first time, and evaluated the performance and potential of GAGG by comparing neutron images obtained using GAGGs with different thicknesses and a P43 scintillator.

2. Materials and Methods

2.1. Neutron-Imaging System and Experimental Conditions

Experiments were performed at the energy-resolved neutron-imaging system RADEN, which was installed at beamline number 22 (BL22) in the Materials and Life Science Experimental Facility (MLF) of the Japan Proton Accelerator Research Complex (J-PARC) [20]. This instrument is equipped with several neutron detectors and have achieved a minimum spatial resolution of 30 μm using a $^6\text{LiF}/\text{ZnS}$ scintillator and a cooled Charge Coupled Device (CCD) camera. For this study, we newly prepared an imaging system, which was originally designed for X-ray imaging with a spatial resolution of less than 10 μm . A schematic of the imaging system is shown in Figure 1. This system consisted of a Complementary Metal–Oxide–Semiconductor (CMOS) camera, two optical lenses, a mirror, and a scintillator. The CMOS camera is an ORCA-Flash4.0 V3 of Hamamatsu Photonics K.K. (Hamamatsu, Japan) with 2048×2048 pixels of 6.5 μm square sensors. The two lenses composed an infinity-corrected optical system [13,14]. The primary lens was 50 mm F1.4 from Nikon (Tokyo, Japan), and, for the secondary lens, we used a 50 mm F1.4 lens and a 105 mm F2.8 lens, both from Nikon, to change the image magnification to 1.0 and 2.1, respectively. These lens conditions are referred to as the “1 \times ” and “2 \times ” conditions hereafter. The fields of view (FoV) are 13.3 mm square and 6.6 mm square, respectively. Two GAGG scintillators, which were commercial products for X-ray imaging, with thicknesses of 10 and 100 μm , were adopted in the experiment, and a P43 with 10 μm thickness was also used for comparison. The diameter of the GAGG scintillator was 15 mm and it was supported by a 1 mm-thick amorphous carbon backplate, while that of the P43 screen was 16 mm, whose substrate was a 0.5 mm-thick beryllium plate. All scintillators were purchased from Hamamatsu Photonics K.K. A Siemens star target made of Gd thin film evaporated onto a quartz substrate from PSI, whose inner line pair was 20 μm wide and whose outer was 500 μm wide [21], was used to evaluate the spatial resolution performance. This target was directly attached to a support plate of a scintillator to minimize geometrical blurring.

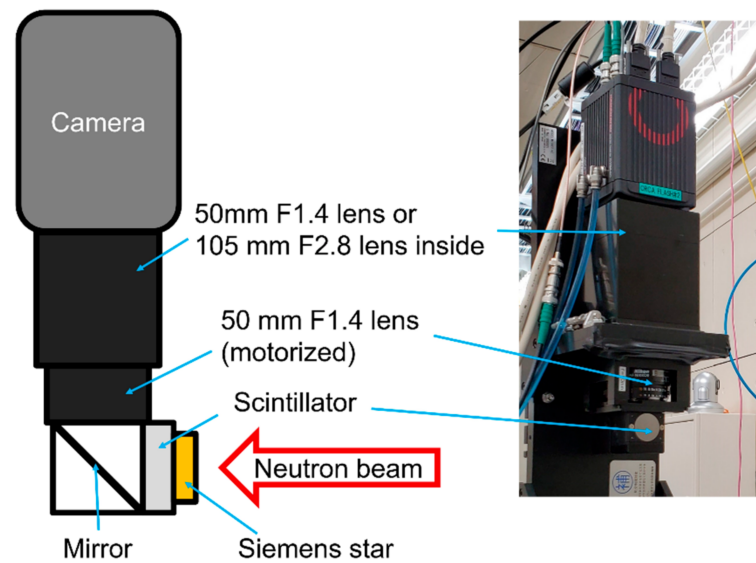


Figure 1. Schematic and picture of the experimental setup.

The $1\times$ experiments were conducted at the far sample position of RADEN located 23 m away from the source. The L/D values, which were related to the beam divergence and, hence, to the spatial resolution, defined by the distance L between the aperture and the sample and the aperture diameter D were 230 and 400. The expected neutron fluxes for L/D of 230 and 400 were 1.0×10^7 and 3.4×10^6 n/s/cm², respectively. In contrast, the $2\times$ experiments were conducted at the near sample position, which was 18 m away from the source, and the L/D values were 180 and 300, respectively. This is because approaching the source allows us to select a smaller L/D , which provides larger neutron flux, and compensates for the decrease of effective neutron intensity according to the decrease of the FoV by $2\times$ image magnification. The neutron fluxes for L/D of 180 and 300 were 1.7×10^7 and 6.1×10^6 n/s/cm², respectively. The accumulation times were $10\text{ s} \times 90$ times for $L/D = 180$ and 230 and $10\text{ s} \times 180$ times for $L/D = 300$ and 400 . For suppression of the white spots in the obtained images, median filtering was applied on the accumulated images but not within the plane of the image. Then, the transmission image was obtained by dark current correction and open-beam normalization. For both experiments, the neutron wavelength range was adjusted from 1.50 to 6.48 Å by using a disk chopper.

2.2. Methods for Calculating Spatial Resolution

The spatial resolution of the images was calculated on the basis of the modulator transfer function (MTF). MTF is obtained by the Fourier transform of the line spread function (LSF), which is the derivative of the edge spread function (ESF). By selecting the fitting function appropriately, the resolution can be analytically calculated with parameters from fitting the ESF. Various types of unsharpness caused by sample vibration, neutron diffusion, scintillator, camera, and so on are expressed as unique functions [22–24]. LSF is generally approximated as Gaussian by convolution of functions of all unsharpness on the basis of the central limit theorem [22,23]. In high-resolution imaging, the unsharpness of the scintillator represented as Lorentzian affects the total unsharpness significantly [23]. Therefore, we adopted the Voigt function, which is a convolution of Gaussian and Lorentzian, as the fitting function. The integral form of the Voigt function was used to fit the ESFs as:

$$V(x) = \text{Re} \left[\frac{1}{2} + \frac{1}{2} \text{erf}(z(x)) + \frac{i(z(x))^2}{\pi} {}_2F_2 \left(1, 1; \frac{3}{2}, 2; -(z(x))^2 \right) \right]. \quad (1)$$

The variable $z(x)$ is expressed as:

$$z(x) = \frac{\sqrt{\pi}}{Bw(i\rho)}(x - \mu) + i\rho. \tag{2}$$

${}_2F_2$ is a generalized hypergeometric function, and $w(x)$ is the Faddeeva function. The parameters are defined as follows: i is the imaginary unit, μ is the inflection point, B is the integral width, and ρ is the Lorentzian contribution. With the fitting parameters and the conversion factor d ($\mu\text{m}/\text{pixel}$), the 10% MTF resolution δ_{MTF} can be represented as:

$$\delta_{MTF} = \frac{d}{2} \frac{\sqrt{\pi}Bw(i\rho)}{(-\rho + \sqrt{\rho^2 + \ln 10})}. \tag{3}$$

In this study, d was defined by dividing the element size of the CMOS camera ($6.5 \mu\text{m}$) by the image magnification. It should be noted that the MTF-based resolution was originally defined as per line pair [7,14] but we applied the resolution per one line to obtain values close to visual observation according to a previous paper [6].

As shown in Figure 2a, in order to average over a sufficiently large area, ESFs were obtained from the outer shell of the Siemens star. Then, the resolutions were calculated from the fitting parameters of ESFs by the method in this section.

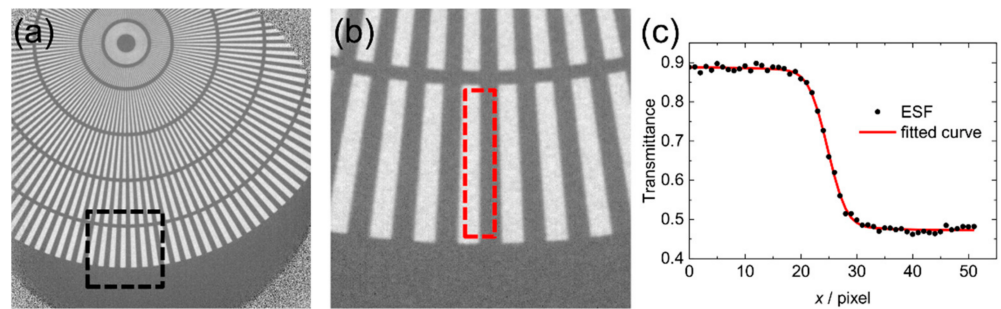


Figure 2. Process of obtaining ESF from a neutron transmission image: (a) whole image example, (b) enlargement of the dashed area in (a), (c) ESF of the dashed area in (b) and fitting curve.

3. Results and Discussion

The performance of each scintillator was evaluated by using the Siemens star target with the optical magnification and L/D as variables. First, the $1\times$ experiments using the 50 mm F1.4 lens for the secondary lens were conducted with GAGG ($100 \mu\text{m}$) and P43 ($10 \mu\text{m}$) scintillators. The obtained transmission images are shown in Figure 3. Because the scintillator could not cover the full area of the FoV in the $1\times$ condition, the four corners of the image did not contribute to the neutron transmission image. Although $20 \mu\text{m}$ -wide line pairs at the center of the Siemens star pattern were not distinguished with either scintillator, as seen in Figure 3, the inner line pairs were more distinguishable by using the GAGG than when by using the P43 scintillator. This was demonstrated by the evaluated MTF values, shown in Table 1. Thus, this experimental result shows that the GAGG could achieve a better spatial resolution than the P43, despite the 10-times-larger thickness, which was a confirmation of the superior performance of the transparent single-crystal scintillator. The change in MTF values for different L/D is discussed later.

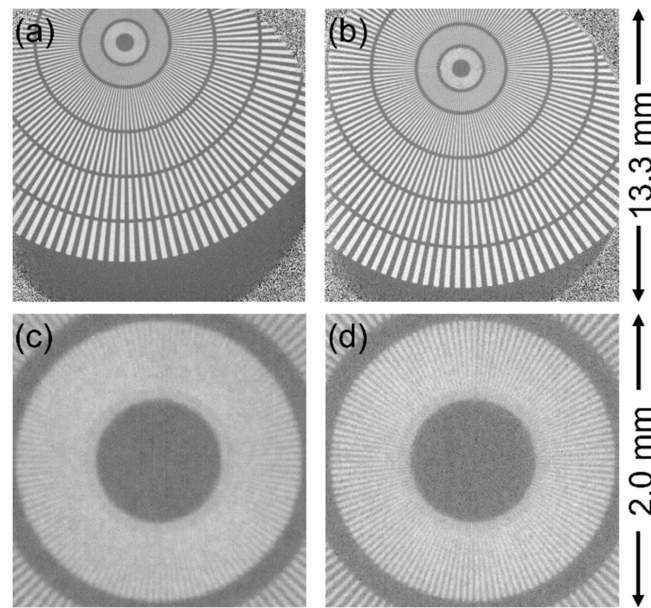


Figure 3. Neutron transmission images taken at $1\times$ magnification condition with $L/D = 400$. (a) An image taken with P43 ($10\ \mu\text{m}$), (b) an image taken with GAGG ($100\ \mu\text{m}$). (c) and (d) are enlarged images of (a) and (b), respectively.

Table 1. Summary of the spatial resolution of neutron radiography of the Siemens star test pattern.

Magnification	Spatial Resolution/ μm			
	$1\times$		$2\times$	
FoV/ mm^2	13.3×13.3		6.6×6.6	
L/D	230	400	180	300
P43 ($10\ \mu\text{m}$)	23.8	25.5	12.9	13.8
GAGG ($100\ \mu\text{m}$)	16.6	15.0	13.0	10.5
GAGG ($10\ \mu\text{m}$)			12.6	11.7

Next, the $2\times$ experiments using the 105 mm F2.8 lens for the secondary lens were conducted. The entire FoV was within the effective area of scintillators in this condition. According to the results of the $1\times$ condition that the GAGG scintillator was confirmed to produce enough light by neutrons, we also employed a $10\text{-}\mu\text{m}$ -thick GAGG scintillator anticipating a higher spatial resolution than the $100\text{-}\mu\text{m}$ -thick one in addition to the scintillators used in the former experiments. Figure 4 shows the neutron transmission images at $L/D = 300$ in the $2\times$ condition for three scintillators. The $10\text{-}\mu\text{m}$ -wide lines in the center of the Siemens star pattern were successfully distinguished by using all scintillators. The image taken with the GAGG ($100\ \mu\text{m}$), shown in Figure 4b,e, appeared as clear as that taken with the P43 scintillator (Figure 4a,d), similar to the results of the $1\times$ condition. By using the $10\text{-}\mu\text{m}$ -thick GAGG scintillator, which should cause the lowest photon scattering and attenuation, the contrast of the image appeared to be further enhanced, as seen in Figure 4c,f. Actually, the Michelson contrast of P43, $100\text{-}\mu\text{m}$ -thick GAGG, and $10\text{-}\mu\text{m}$ -thick GAGG was calculated to be 45%, 44%, and 57%, respectively.

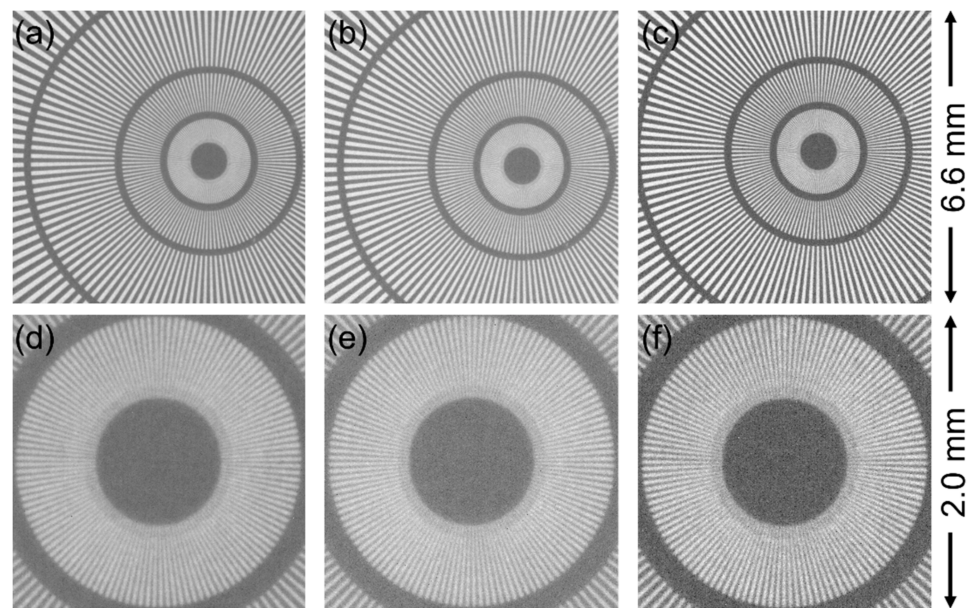


Figure 4. High-resolution neutron radiography taken at $2\times$ magnification under $L/D = 300$ conditions by three types of scintillators: (a) an image taken with P43 ($10\ \mu\text{m}$), (b) an image taken with GAGG ($100\ \mu\text{m}$), (c) an image taken with GAGG ($10\ \mu\text{m}$), (d) an enlarged view of (a), (e) an enlarged view of (b), and (f) an enlarged view of (c).

The resolution derived from Figure 4 is summarized in Table 1. The best resolution of $10.5\ \mu\text{m}$ was achieved by using the GAGG ($100\ \mu\text{m}$) at $2\times$ magnification under $L/D = 300$ condition. Despite the thinness, the $10\text{-}\mu\text{m}$ -thick GAGG scintillator did not achieve the highest spatial resolution. The reasons for this inferior performance compared to the thicker GAGG are nonuniformity of the image and difficulty in focus adjustment due to the small light yield.

Here, we will mention the difference in MTF-based resolution with the different L/D s. In general, a large L/D decreases neutron flux but allows access to a fine spatial resolution. This characteristic could be found in the study using GAGG scintillators, and higher resolutions could be obtained with larger L/D s. Conversely, the results with the P43 scintillator did not follow this rule. The reason is not clear, but may be due to the insufficient focus adjustment, and hence, a failure to correctly recognize the difference in MTF values. The precise focus adjustment is essential for achieving higher resolution and for a fair comparison among the scintillators. However, the fact that the $100\text{-}\mu\text{m}$ -thick GAGG scintillator could achieve $10\ \mu\text{m}$ resolution still strongly supports the superior performance of the transparent single-crystal scintillator.

The effective luminance histograms per 10 s for each scintillator, which were calculated by subtracting the background luminance from the direct beam luminance of $2\times$ experiments, are shown in Figure 5. This figure indicates that the GAGG scintillator with $100\ \mu\text{m}$ thickness was about half as luminant as the P43, and the GAGG with $10\ \mu\text{m}$ thickness was half of that. From the composition of each scintillator, the attenuation coefficients for thermal neutrons can be calculated to be $1157.0\ \text{cm}^{-1}$ and $642.1\ \text{cm}^{-1}$ for P43 and GAGG, respectively. Then, the thermal neutron transmission was assumed to be 31.4% for the $10\text{-}\mu\text{m}$ -thick P43, 0.162% for the $100\text{-}\mu\text{m}$ -thick GAGG, and 52.0% for the $10\text{-}\mu\text{m}$ -thick GAGG scintillator. Hence, the different effective luminance between GAGGs can be easily understood from the different amounts of the absorbed neutrons. This also implies that the self-attenuation of emitted light was negligibly small. Considering the effective luminance normalized with the neutron attenuation rate, the P43 was three times brighter than the GAGG. Although the light emission performance of GAGG for neutron irradiation was expected to be comparable to that of P43 considering the results of X-ray irradiation [17,25], it was revealed that there was a large difference between the two scintillators in reality.

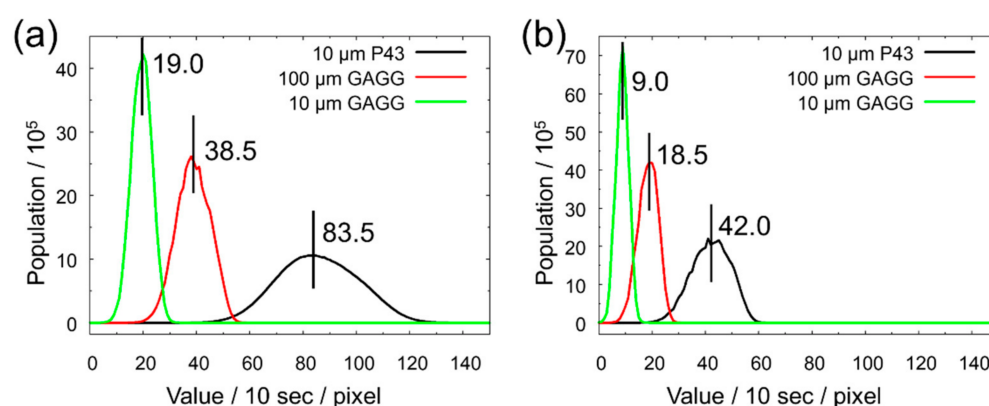


Figure 5. Histograms of open-beam intensity taken at $2\times$ magnification with scintillators P43 ($10\ \mu\text{m}$), GAGG ($100\ \mu\text{m}$), and GAGG ($10\ \mu\text{m}$): (a) $L/D = 180$ and (b) $L/D = 300$. The position and value of the median are shown in the figure.

Finally, we discuss the prospects of the high-spatial-resolution neutron imaging with the GAGG scintillator. The current performance of the GAGG does not fully surpass that of the P43. However, the GAGG still has room to improve its performance as a neutron scintillator because the GAGG used in this study is not optimized for neutron application but for X-ray experiments. The decay time of emitted light is too short, and considering the X-ray energy resolution is not necessary. Therefore, material design to increase the light yield by neutron irradiation will make the GAGG a good neutron scintillator, for example, by selecting doping elements and optimizing their amounts to generate suitable emission centers similar to studies conducted for X-ray use [26–28], or adjusting matrix crystal composition to exhibit an appropriate band gap and high enough Gd concentration. Owing to increase in the light yield, the GAGG will be a good alternative candidate to Gadox enriched with ^{157}Gd isotope. Because of its transparency and small light scattering, the GAGG can be made thicker to increase the efficiency without degrading the resolution. Then, both scintillators will produce comparable luminance. Because the GAGG does not need to be enriched with isotopes, it can reduce the cost substantially. Moreover, a newly developed 4-inch GAGG single crystal will enable imaging with a larger FoV [29]. Those will make a significant contribution to conducting high-resolution neutron imaging more easily.

4. Conclusions

The transparent single-crystal GAGG scintillator, which was developed for X-ray radiography, was used in neutron radiography for the first time and achieved a spatial resolution of $10.5\ \mu\text{m}$. The $100\text{-}\mu\text{m}$ -thick GAGG scintillator showed higher spatial resolution than that of the $10\text{-}\mu\text{m}$ -thick P43 powder scintillator because transparent single-crystal scintillators reduce internal scattering and attenuation of light regardless of thickness. These results provide potential for an inexpensive high-resolution scintillator without a ^{157}Gd isotope. By optimizing the composition of GAGG to the neutron use, high-resolution neutron imaging will be more common.

Author Contributions: Conceptualization, K.I., D.S., H.K. and T.S.; methodology, K.I., D.S., H.K. and T.S.; software, K.I. and T.S.; validation, K.I., D.S. and T.S.; formal analysis, K.I. and T.S.; investigation, K.I. and T.S.; resources, T.S.; data curation, K.I.; writing—original draft preparation, K.I.; writing—review and editing, K.I., D.S., H.K. and T.S.; visualization, K.I.; supervision, T.S.; project administration, T.S. All authors have read and agreed to the published version of the manuscript.

Funding: This research received no external funding.

Institutional Review Board Statement: Not applicable.

Informed Consent Statement: Not applicable.

Data Availability Statement: Not applicable.

Acknowledgments: The authors would like to thank Y. Nagai of Toyota Central R&D Laboratories, K. Kurita of Japan Atomic Energy Agency, and the RADEN team members for their useful advice and assistance. This experiment has been performed under a user program (Proposal Number 2019I0022) in the MLF of the J-PARC. The authors would like to thank Enago (www.enago.jp (accessed on 1 November 2021)) for the English language review.

Conflicts of Interest: The authors declare no conflict of interest.

References

1. Boillat, P.; Lehmann, E.H.; Trtik, P.; Cochet, M. Neutron imaging of fuel cells—Recent trends and future prospects. *Curr. Opin. Electrochem.* **2017**, *5*, 3–10. [[CrossRef](#)]
2. Liu, D.Q.; Shadike, Z.; Lin, R.Q.; Qian, K.; Li, H.; Li, K.K.; Wang, S.W.; Yu, Q.P.; Liu, M.; Ganapathy, S.; et al. Review of recent development of in situ/operando characterization techniques for lithium battery research. *Adv. Mater.* **2019**, *31*, 1806620. [[CrossRef](#)] [[PubMed](#)]
3. Morgano, M.; Trtik, P.; Meyer, M.; Lehmann, E.H.; Hovind, J.; Strobl, M. Unlocking high spatial resolution in neutron imaging through an add-on fibre optics taper. *Opt. Express* **2018**, *26*, 1809–1816. [[CrossRef](#)]
4. Trtik, P.; Lehmann, E.H. Progress in high-resolution neutron imaging at the Paul Scherrer Institut—The neutron microscope project. *J. Phys. Conf. Ser.* **2016**, *746*, 012004. [[CrossRef](#)]
5. Trtik, P.; Meyer, M.; Wehmann, T.; Tengattini, A.; Atkins, D.; Lehmann, E.H.; Strobl, M. PSI ‘neutron microscope’ at ILL-D50 beamline—First results. *Mater. Res. Proc.* **2020**, *15*, 23–28.
6. Minniti, T.; Tremsin, A.S.; Vitucci, G.; Kockelmann, W. Towards high-resolution neutron imaging on IMAT. *J. Instrum.* **2018**, *13*, C01039. [[CrossRef](#)]
7. Borges, N.P.; Losko, A.S.; Vogel, S.C. Event centroiding applied to energy-resolved neutron imaging at LANSCE. *J. Imaging* **2018**, *4*, 40. [[CrossRef](#)]
8. Hussey, D.S.; LaManna, J.M.; Baltic, E.; Jacobson, D.L. Neutron imaging detector with 2 μm spatial resolution based on event reconstruction of neutron capture in gadolinium oxysulfide scintillators. *Nucl. Instrum. Methods Phys. Res. A* **2017**, *866*, 9–12. [[CrossRef](#)]
9. Faenov, A.; Matsubayashi, M.; Pikuz, T.; Fukuda, Y.; Kando, M.; Yasuda, R.; Iikura, H.; Nojima, T.; Sakai, T.; Shiozawa, M.; et al. Using LiF crystals for high-performance neutron imaging with micron-scale resolution. *High Power Laser Sci. Eng.* **2015**, *3*, e27. [[CrossRef](#)]
10. Hirota, K.; Ariga, T.; Hino, M.; Ichikawa, G.; Kawasaki, S.; Kitaguchi, M.; Mishima, K.; Muto, N.; Naganawa, N.; Shimizu, H.M. Neutron imaging using a fine-grained nuclear emulsion. *J. Imaging* **2021**, *7*, 4. [[CrossRef](#)]
11. Liu, D.; Hussey, D.; Gubarev, M.V.; Ramsey, B.D.; Jacobson, D.; Arif, M.; Moncton, D.E.; Khaykovich, B. Demonstration of achromatic cold-neutron microscope utilizing axisymmetric focusing mirrors. *Appl. Phys. Lett.* **2013**, *102*, 183508. [[CrossRef](#)]
12. Graafsma, H.; Martin, T. Detectors for synchrotron tomography. In *Advanced Tomographic Methods in Materials Research and Engineering*; Banhart, J., Ed.; Oxford University Press: Oxford, UK, 2008; pp. 277–302.
13. Tengattini, A.; Lenoir, N.; Andò, E.; Giroud, B.; Atkins, D.; Beaucour, J.; Viggiani, G. NeXT-Grenoble, the neutron and X-ray tomograph in Grenoble. *Nucl. Instrum. Methods Phys. Res. A* **2020**, *968*, 163939. [[CrossRef](#)]
14. Williams, S.H.; Hilger, A.; Kardjilov, N.; Manke, I.; Strobl, M.; Douissard, P.A.; Martin, T.; Riesemeier, H.; Banhart, J. Detection system for microimaging with neutrons. *J. Instrum.* **2012**, *7*, P02014. [[CrossRef](#)]
15. Kamada, K.; Yanagida, T.; Endo, T.; Tsutumi, K.; Usuki, Y.; Nikl, M.; Fujimoto, Y.; Yoshikawa, A. 2-inch size single crystal growth and scintillation properties of new scintillator; Ce:Gd₃Al₂Ga₃O₁₂. In Proceedings of the 2011 IEEE Nuclear Science Symposium Conference Record, Valencia, Spain, 23–29 October 2011; pp. 1927–1929.
16. Kamada, K.; Yanagida, T.; Endo, T.; Tsutumi, K.; Usuki, Y.; Nikl, M.; Fujimoto, Y.; Fukabori, A.; Yoshikawa, A. 2 inch diameter single crystal growth and scintillation properties of Ce:Gd₃Al₂Ga₃O₁₂. *J. Cryst. Growth* **2012**, *352*, 88–90. [[CrossRef](#)]
17. Kurosawa, S.; Shoji, Y.; Yokota, Y.; Kamada, K.; Chani, V.I.; Yoshikawa, A. Czochralski growth of Gd₃(Al_{5-x}Ga_x)O₁₂ (GAGG) single crystals and their scintillation properties. *J. Cryst. Growth* **2014**, *393*, 134–137. [[CrossRef](#)]
18. Sharma, S.K.; Som, S.; Jain, R.; Kunti, A.K. Spectral and CIE parameters of red emitting Gd₃Ga₅O₁₂:Eu³⁺ phosphor. *J. Lumin.* **2015**, *159*, 317–324. [[CrossRef](#)]
19. Taggart, M.P.; Nakhostin, M.; Sellin, P.J. Investigation into the potential of GAGG:Ce as a neutron detector. *Nucl. Instrum. Methods Phys. Res. A* **2019**, *931*, 121–126. [[CrossRef](#)]
20. Shinohara, T.; Kai, T.; Oikawa, K.; Nakatani, T.; Segawa, M.; Hiroi, K.; Su, Y.; Ooi, M.; Harada, M.; Iikura, H.; et al. The energy-resolved neutron imaging system, RADEN. *Rev. Sci. Instrum.* **2020**, *91*, 043302. [[CrossRef](#)] [[PubMed](#)]
21. Grünzweig, C.; Frei, G.; Lehmann, E.; Kühne, G.; David, C. Highly absorbing gadolinium test device to characterize the performance of neutron imaging detector systems. *Rev. Sci. Instrum.* **2007**, *78*, 053708. [[CrossRef](#)] [[PubMed](#)]
22. Spiegler, P.; Norman, A. The total unsharpness in radiography. *Phys. Med. Biol.* **1973**, *18*, 884–887. [[CrossRef](#)] [[PubMed](#)]
23. Harms, A.A.; Wyman, D.R. *Mathematics and Physics of Neutron Radiography*; D. Reidel Publishing Company: Dordrecht, The Netherlands, 1986; pp. 27–43.

24. Tobin, K.W.; Bingham, P.R.; Gregor, J. Mathematics of neutron imaging. In *Neutron Imaging and Applications*; Anderson, I.S., McGreevy, R., Bilheux, H.Z., Eds.; Springer: Berlin, Germany, 2009; pp. 109–127.
25. Martin, T.; Douissard, P.-A.; Seeley, Z.; Cherepy, N.; Payne, S.; Mathieu, E.; Schuladen, J. New high stopping power thin scintillators based on Lu_2O_3 and $\text{Lu}_3\text{Ga}_{5-x}\text{In}_x\text{O}_{12}$ for high resolution X-ray imaging. *IEEE Trans. Nuclear Sci.* **2012**, *59*, 2269–2274. [[CrossRef](#)]
26. Chewpraditkul, W.; Pattanaboonmee, N.; Sakthong, O.; Chewpraditkul, W.; Yoshino, M.; Horiai, T.; Yoshikawa, A.; Gushchina, L.; Kamada, K.; Kurosawa, S.; et al. Luminescence and scintillation properties of Mg^{2+} -codoped $\text{Lu}_{0.6}\text{Gd}_{2.4}\text{Al}_2\text{Ga}_3\text{O}_{12}:\text{Ce}$ single crystal. *IEEE Trans. Nuclear Sci.* **2020**, *67*, 904–909. [[CrossRef](#)]
27. Kozlova, N.S.; Buzanov, O.A.; Kasimova, V.M.; Kozlova, A.P.; Zabelina, E.V. Optical characteristics of single crystal $\text{Gd}_3\text{Al}_2\text{Ga}_3\text{O}_{12}:\text{Ce}$. *Mod. Electron. Mater.* **2018**, *4*, 7–12. [[CrossRef](#)]
28. Kasimova, V.M.; Kozlova, N.S.; Buzanov, O.A.; Zabelina, E.V. Effect of Ca^{2+} and Zr^{4+} co-doping on the optical properties of $\text{Gd}_3\text{Al}_2\text{Ga}_3\text{O}_{12}:\text{Ce}$ single crystals. *Mod. Electron. Mater.* **2019**, *5*, 101–105. [[CrossRef](#)]
29. Kochurikhin, V.; Kamada, K.; Kim, K.; Ivanov, M.; Gushchina, L.; Shoji, Y.; Yoshino, M.; Yoshikawa, A. Czochralski growth of 4-inch diameter Ce: $\text{Gd}_3\text{Al}_2\text{Ga}_3\text{O}_{12}$ single crystals for scintillator applications. *J. Cryst. Growth* **2020**, *531*, 125384. [[CrossRef](#)]